PHYSICAL REVIEW B **103**, 024437 (2021)

Chirality-induced linear response properties in noncoplanar Mn_3Ge

Sebastian Wimmer,[*] Sergiy Mankovsky, and Hubert Ebert
Department Chemie, Physikalische Chemie, Universität München, Butenandtstrasse 5-13, 81377 München, Germany

(Received 28 April 2020; revised 27 November 2020; accepted 4 January 2021; published 22 January 2021)

Taking the noncollinear antiferromagnetic hexagonal Heusler compound Mn_3Ge as a reference system, the contributions to linear response phenomena arising solely from the chiral coplanar and noncoplanar spin configurations are investigated. Orbital moments, x-ray absorption, and anomalous and spin Hall effects, as well as corresponding spin-orbit torques and Edelstein polarizations, are studied depending on a continuous variation of the polar angle relative to the kagome planes of corner-sharing triangles between the noncollinear antiferromagnetic and the ferromagnetic limits. By scaling the speed of light from the relativistic Dirac case to the nonrelativistic limit the chirality-induced or topological contributions can be identified by suppressing the spin-orbit coupling.

DOI: 10.1103/PhysRevB.103.024437

I. INTRODUCTION

Chiral magnetic order, its origins and consequences, continues to be a fascinating area of current solid state science [1–5]. Particularly intriguing is the occurrence of mesoscopic quasiparticles formed by a continuously varying noncoplanar spin texture with defined topology, so-called skyrmions [6–8]. Their properties, creation, detection, and manipulation make up a very active field of research [9–14], motivated by potential future applicability in magnetic storage [15–18]. Electric-field-induced transport plays an important role in this context, as corresponding charge and spin currents can be utilized to detect and manipulate skyrmions [15,16,19] and antiskyrmions [20]. Due to the noncoplanar spin texture a so-called emergent electromagnetic field arises that leads to chirality-induced or *topological*, in the sense of arising from the real-space topology of the spin configuration, contributions to phenomena commonly associated with spin-orbit coupling. The most fundamental of them are the occurrence of topological orbital moments [21–26] and of the related topological Hall effect (THE) [27–34]. A corresponding spin Hall effect arising from the real-space topology of the spin texture [35] is of particular interest in antiferromagnetic skyrmions, where the THE vanishes [36].

A second intensively investigated type of chiral magnetic order is that of bulk antiferromagnets with noncollinear spin arrangements. The anomalous Hall effect (AHE) has been studied extensively in such compounds both theoretically [21,31,37–39] and experimentally [40–46]. Its relation to the magneto-optic Kerr effect of chiral magnets [47,48] and the x-ray circular dichroism [25,49], both connected to the optical conductivity tensor, suggests an alternative, magneto-optical approach to noncollinear magnetic order. Of particular relevance to the field are the hexagonal Heusler compounds Mn_3X with X = Ga, Ge, and Sn, in which the AHE has recently been confirmed experimentally [42–44]. Its spin-polarized counterpart, the spin Hall effect (SHE), in these and other noncollinear antiferromagnets also stimulated theoretical efforts [39,50–52] and has been measured in the achiral cubic system Mn_3Ir [53,54]. In Ref. [54] it has been furthermore shown that the SHE contributes to the so-called spin-orbit torque (SOT), the current-induced magnetic torque that can be utilized to efficiently switch the magnetization. Thermally induced analogs to the AHE and SHE, the anomalous and spin Nernst effects have been studied in Mn_3X (X = Sn, Ge, Ga) from first principles using the Berry curvature approach and a Mott-like formula [55]. The anomalous Nernst effect has in fact been measured recently in Mn_3Sn [56].

The merger of these two fields called *topological antiferromagnetic spintronics* [57] aims to explore the potential of topologically protected quasiparticles with nontrivial real- or momentum-space topology. This work contributes to this by a first-principles study on the chirality-induced or topological contributions to orbital moments, x-ray absorption spectra, and anomalous and spin Hall effects, as well as to spin-orbit torques and the closely related Edelstein effect (EE). Two coplanar noncollinear antiferromagnetic spin structures in Mn_3Ge, one chiral and the other achiral, are used as the basis for investigations on the impact of noncoplanarity by rotating the magnetic moments out of the kagome planes. Scaling the speed of light allows assessing the topological contributions to the various effects in the absence of spin-orbit coupling. This is accompanied by an analysis of the corresponding symmetry-restricted response tensor shapes.

The manuscript is organized as follows. In Sec II the underlying methods used for obtaining the results in Sec. III are outlined. The crystallographic and magnetic structures are discussed in Sec. III A, including the corresponding symmetry-restricted tensor shapes for electrical and spin conductivity as well as spin-orbit torkance and Edelstein polarization. Topological orbital moments and their signatures in x-ray absorption spectra are the subjects of Secs. III B and III C, respectively. The chirality-induced contributions to the anomalous and spin Hall effects are discussed

---

[*] Present address: Max-Planck-Gesellschaft, CPTS, Postfach 101062, 80064 München, Germany.

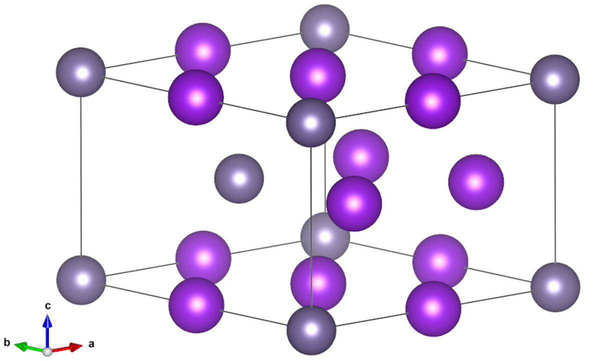

FIG. 1. Hexagonal unit cell of Mn_3Ge with the space group $P6_3/mmc$ (labeled NM in the following). The Mn atoms on the Wyckoff positions $6h$ are colored in magenta (dark gray) and Ge atoms (Wyckoff positions $2h$) are colored in light gray [77].

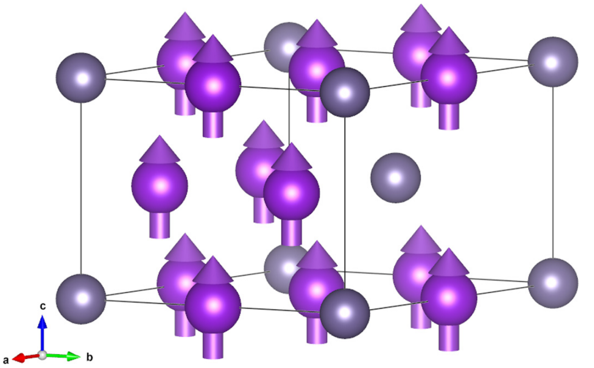

FIG. 2. Unit cell of hexagonal ferromagnetic (FM) Mn_3Ge with the magnetic space group $P6_3/mm'c'$. The use of colors is the same as in Fig. 1; magnetic moments on Mn sites are indicated as vectors [77].

in Sec. III D; the corresponding results for the spin-orbit torque and the Edelstein effect are presented in Sec. III E. Finally, hypothetical noncoplanar antiferromagnets are investigated in Sec. III F. A brief summary and outlook are made at the end (Sec. IV), and additional information can be found in the Appendix.

II. METHODS

The space-time symmetry analysis of the linear response tensors for charge [58,59] and spin conductivity [59], spin-orbit torque [60], and Edelstein polarization [61] performed in this work is based on the magnetic space group determined using the software FINDSYM [62,63]. Calculations for the corresponding linear response quantities have been done on the basis of Kubo's linear response formalism [64–68]. As has been demonstrated many times, this approach is completely equivelent to the use of expressions based on the Berry curvature [69–72]. In contrast to the latter one, however, implementing the Kubo formalism by representing the electronic structure in terms of its retarded Green function allows straightforward application to disordered materials [71,72]. All numerical work has been done in a fully relativistic way using the spin-polarized relativistic Korringa-Kohn-Rostoker (SPR-KKR) [73] electronic structure method within the framework of the local spin density approximation. Explicit expressions used for the calculations of the response functions can be found in the literature (charge conductivity [64–66], spin conductivity [67,68], spin-orbit torkance [60], the Edelstein effect [61], and the x-ray absorption formalism [74]) For the calculation of electric-field-induced response properties the Kubo-Středa [75] formula has been used throughout. To study the impact of the spin texture in the absence of spin-orbit coupling, the nonrelativistic limit of the Dirac formalism has been explored by scaling the speed of light [76].

III. RESULTS

A. Magnetic structure and symmetry

The hexagonal Mn_3Ge compound crystallizes, as its siblings Mn_3Sn and Mn_3Ga, in the $D0_{19}$ structure with the space group $P6_3/mmc$. The nonmagnetic unit cell is shown in Fig. 1 and is labeled NM in the following. The Mn atoms on the Wyckoff positions $6h$ in the $\{0001\}$ planes colored in magenta (dark gray) form triangular, so-called kagome lattices, stacked alternatingly along the $[0001]$ (z) direction. Ge atoms occupying the Wyckoff positions $2h$ are colored in light gray. Figure 2 shows the situation of a field-aligned ferromagnetic structure with all moments (only shown for Mn sites) oriented along the $[0001]$ or z direction (c axis of the unit cell). The corresponding magnetic space group is $P6_3/mm'c'$. This structure is labeled FM in the following.

A number of noncollinear but coplanar antiferromagnetic alignments of the moments have been discussed for Mn_3Ge and related compounds in the literature (cf. Ref. [78] and references therein). Recently an overview on the properties of actual and hypothetical spin-compensated configurations has been given by the present authors [49]. Two coplanar ones of these structures discussed therein, both hypothetical, are shown in Fig. . The one in Fig. 3(a), labeled ncAFM0 in accordance with Ref. [49], has the moments in the two alternating kagome planes, indicated by different colors (red and blue), pointing towards the center of the triangles formed by the Mn atoms. The two magnetic sublattices are connected, e.g., by a 6_3 screw rotation about an axis going through the center of both triangles, but also by inversion with respect to the midpoint between these centers followed by time reversal. Reversing all moments in one layer (here blue), one obtains the structure ncAFM9 shown in the bottom panel. Here the operation connecting the two sublattices involves an additional time reversal ($6'_3$), leading to a centrosymmetric or achiral structure with an inversion center halfway along c. Both structures serve as references for the investigations on the consequences of noncoplanarity of the Mn moments in this work.

Rotation of the moments out of both kagome planes by the same polar angle θ between the $[0001]$ direction and the $\{0001\}$ planes leads for $\theta = 45^\circ$ to the noncoplanar spin arrangements depicted in Fig. 4. The one in Fig. 4(a), ncpM0 derived from ncAFM0, is obviously still chiral. The structure derived from ncAFM9, labeled ncpM9 and shown in Fig. 4(b), accordingly remains achiral; the inversion center connecting the two sublattices is indicated by an orange dot.

The main aim of the present work is the numerical study of chirality-induced or *topological* effects in transport and

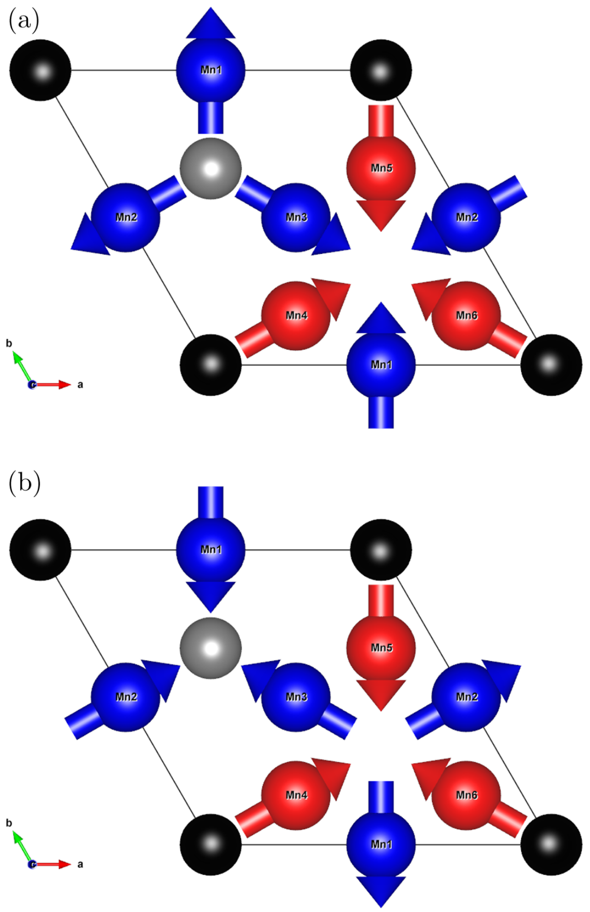

FIG. 3. Noncollinear coplanar (nc) antiferromagnetic reference structures of Mn_3Ge, ncAFM0 (a) and ncAFM9 (b). The coplanar Mn moments in alternating kagome planes are colored red and blue. The achiral structure ncAFM9 in panel (b) is obtained from ncAFM0 by reversing all moments in one plane (blue) [77].

related properties. While the individual kagome sublattices in the antiferromagnetic structures just discussed are chiral, as they have a finite vector spin chirality $\vec{S}_i \times \vec{S}_j + \vec{S}_j \times \vec{S}_k + \vec{S}_k \times \vec{S}_i$, the anomalous Hall conductivity arising from this is vanishing globally. This can be unambiguously derived from the space-time symmetry properties of the current-current correlation function in terms of the Kubo formula behavior for the electrical conductivity [58]. The transformation under all symmetry operations of the so-called magnetic Laue group (see Ref. [59] for its definition used here) is sufficient to derive the symmetry-restricted tensor shape. The magnetic space and Laue groups for all spin configurations discussed in this work are given in Table. I. For convenience the Laue group is given also according to the older definition used by Kleiner [58].

The electrical conductivity tensor shapes derived from the corresponding magnetic Laue group are as follows [58,59]:

$$\underline{\sigma}^{\mathrm{NM}} = \begin{pmatrix} \sigma_{xx} & 0 & 0 \\ 0 & \sigma_{xx} & 0 \\ 0 & 0 & \sigma_{zz} \end{pmatrix} = \underline{\sigma}^{\mathrm{ncAFM0,9}} = \underline{\sigma}^{\mathrm{ncpAFM0,9}}, \quad (1)$$

$$\underline{\sigma}^{\mathrm{FM}} = \begin{pmatrix} \sigma_{xx} & \sigma_{xy} & 0 \\ -\sigma_{xy} & \sigma_{xx} & 0 \\ 0 & 0 & \sigma_{zz} \end{pmatrix} = \underline{\sigma}^{\mathrm{ncpM0,9}} . \quad (2)$$

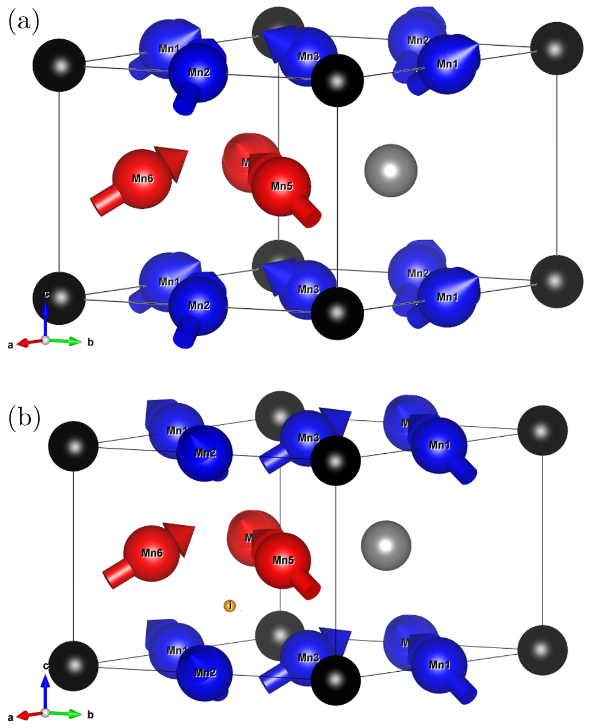

FIG. 4. Noncoplanar (ncp) magnetic structures of Mn_3Ge derived from ncAFM0 and ncAFM9 (see Fig. 3) by rotating the moments out of the kagome planes by $\theta = 45^\circ$. While the one in panel (a), labeled ncpM0, is chiral, the structure ncpM9 in panel (b) has an inversion center that is indicated by an orange dot [77].

As stated above, the noncollinear coplanar antiferromagnetic structures in Fig. 3 have the same conductivity tensor shape as the nonmagnetic one. This applies as well to the noncoplanar antiferromagnetic structures that are discussed in Sec. III F. The noncoplanar magnetic structures of Fig. 4 on the other hand have the same shape of $\underline{\sigma}$ as for the ferromagnetic (FM) case. However, as is shown below, a chirality-induced contribution to the anomalous Hall conductivity $\sigma_{xy} = -\sigma_{yx}$ can be identified here.

TABLE I. Magnetic space (MSG), point (MPG), and Laue (MLG) groups of the magnetic structures shown in Figs. 3 and 4 with nc and ncp standing for noncollinear and noncoplanar, respectively. The Laue groups are given following the standard definition used by Seemann *et al.* [59] as well as the older one used by Kleiner [58] (in parentheses). The conventional setting concerning the sequence of generators is used for the space groups and carried over to the point and Laue groups [79].

Label	MSG	MPG	MLG
NM	$P6_3/mmc1'$	$6/mmm1'$	$6/mmm1'$ $(6221')$
FM	$P6_3/mm'c'$	$6/mm'm'$	$6/mm'm'$ $(62'2')$
ncAFM0	$P6_3/m'm'c'$	$6/m'm'm'$	$6/mmm1'$ $(6221')$
ncAFM9	$P6'_3/m'm'c$	$6'/m'm'm$	$6'/m'm'm$ $(6'22')$
ncpM0	$P6_3m'c'$	$6m'm'$	$6/mm'm'$ $(62'2')$
ncpM9	$P\bar{3}m'1$	$\bar{3}m'1$	$\bar{3}m'1$ $(32')$
ncpAFM0	$P\bar{3}'1m'$	$\bar{3}'1m'$	$\bar{3}1m1'$ $(3'2)$
ncpAFM9	$P6'_3m'c$	$6'm'm$	$6'/m'm'm$ $(6'2'2)$

The corresponding spin conductivity tensor shapes for polarization along the z or [0001] direction are [59] as follows:

$$\underline{\boldsymbol{\sigma}}^{z,\mathrm{NM}} = \begin{pmatrix} 0 & \sigma^z_{xy} & 0 \\ -\sigma^z_{xy} & 0 & 0 \\ 0 & 0 & 0 \end{pmatrix} = \underline{\sigma}^{z,\mathrm{ncAFM0,9}} = \underline{\sigma}^{z,\mathrm{ncpAFM0,9}}, \tag{3}$$

$$\underline{\boldsymbol{\sigma}}^{z,\mathrm{FM}} = \begin{pmatrix} \sigma^z_{xx} & \sigma^z_{xy} & 0 \\ -\sigma^z_{xy} & \sigma^z_{xx} & 0 \\ 0 & 0 & \sigma^z_{zz} \end{pmatrix} = \underline{\sigma}^{z,\mathrm{ncpM0,9}}. \tag{4}$$

The corresponding tensor for polarization along the x and $y0$ directions can be found in Ref. [59]. The antiferromagnetic structures, regardless of whether they are coplanar or noncoplanar, chiral or achiral, show only one independent nonzero element, namely the spin Hall conductivity $\sigma^z_{xy} = -\sigma^z_{yx}$ as in the nonmagnetic case. Note, however, that the tensors for the other two polarization directions differ for the structures ncAFM9, ncpAFM0, and ncpAFM9 (see Ref. [59]). The noncoplanar magnetic structures ncpM0 and ncpM9 have the same tensor shape for $\underline{\boldsymbol{\sigma}}^z$ as the ferromagnetic one. While ncpM0 has the same magnetic Laue group ($6/mm'm'$) and accordingly the same tensor shapes for all $\underline{\boldsymbol{\sigma}}^k$ as the FM structure, the other two polarization directions, x and y, behave again differently for ncpM9. Also here a sizable chirality-induced contribution will be shown to exist.

The Edelstein polarization tensor shapes for the noncentrosymmetric spin configurations ncAFM0, ncpM0, ncpAFM0, and ncpAFM9 are found as follows [61]:

$$\underline{\boldsymbol{p}}^{\mathrm{ncAFM0}} = \begin{pmatrix} p_{xx} & 0 & 0 \\ 0 & p_{xx} & 0 \\ 0 & 0 & p_{zz} \end{pmatrix}, \tag{5}$$

$$\underline{\boldsymbol{p}}^{\mathrm{ncpM0}} = \begin{pmatrix} p_{xx} & p_{xy} & 0 \\ -p_{xy} & p_{xx} & 0 \\ 0 & 0 & p_{zz} \end{pmatrix}, \tag{6}$$

$$\underline{\boldsymbol{p}}^{\mathrm{ncpAFM0}} = \begin{pmatrix} p_{xx} & 0 & 0 \\ 0 & p_{xx} & 0 \\ 0 & 0 & p_{zz} \end{pmatrix}, \tag{7}$$

$$\underline{\boldsymbol{p}}^{\mathrm{ncpAFM9}} = \begin{pmatrix} 0 & p_{xy} & 0 \\ -p_{xy} & 0 & 0 \\ 0 & 0 & 0 \end{pmatrix}. \tag{8}$$

Finally, the shapes of the spin-orbit torkance tensors $\underline{\boldsymbol{t}}$ are identical to the ones given for $\underline{\boldsymbol{p}}$ in Eqs. (5)–(8) [60]. It should be stressed that for these two response properties the tensor shape is determined by the magnetic point group and not by the magnetic Laue group.

B. Orbital moments

The occurrence of chirality-induced orbital moments in noncoplanar spin arrangements has been predicted already quite some time ago [21,22]. First-principles calculations in, e.g., atomic-scale spin lattices [23,24], triatomic clusters of ferromagnetic $3d$ elements on a surface [25], and bulk γ-FeMn [26] could verify these in the limit of vanishing spin-orbit coupling. The (non)coplanarity between three spins can be expressed compactly by the so-called scalar spin chirality $\chi_{ijk} = \vec{S}_i \cdot (\vec{S}_j \times \vec{S}_k)$. If the volume of the parallelepiped spanned by the three spin vectors is nonzero, they obviously are noncoplanar. In Fig. 5 the orbital moment μ_{orb} is shown for ncpM0 as a function of the polar angle θ between the [0001] direction and the {0001} planes. It is the same for all spin magnetic moments in the unit cell. The azimuthal angles ϕ_i corresponding to these spin moments are taken such that $\phi_i - \phi_j = \pm 120^\circ$ for any two in-plane-neighboring Mn atoms i and j. As a result, the effective spin $\vec{\mu}_{\mathrm{spin}}$ and orbital $\vec{\mu}_{\mathrm{orb}}$ magnetic moment defined as the vector sum over all sites in the unit cell are nonzero only for the z component, $\mu_{\mathrm{spin}} = \mu_{spin,z}$ and $\mu_{\mathrm{orb}} = \mu_{\mathrm{orb},z}$, for all spin configurations discussed in the paper. For the tilting angles θ and $-\theta$, the z components of the orbital moments are equal, implying that μ_{orb} is symmetric with respect to a sign change of θ. For the in-plane orientation of the spin magnetic moments, the total spin magnetic moment μ_{spin} is equal to zero, leading to a vanishing orbital magnetic moment μ_{orb}. Tilted up or down from the in-plane situation, the spin magnetic moment μ_{spin} is either positive or negative. Following the spin magnetic moment, the orbital magnetic moment μ_{orb} shows the same trend, as can be seen in Fig. 5. In the case of vanishing spin-orbit coupling (no SOC, open circles) the remaining chirality-induced contribution to the orbital moment can indeed be fairly well fitted with a function $\propto \cos(\theta)\sin^2(\theta)$ reflecting the scalar spin chirality $\chi_{ijk}(\theta)$. The zeros of this function correspond to the ferromagnetic state ($\theta = 0^\circ, 180^\circ$) and the noncollinear antiferromagnetic state ($\theta = -90^\circ, 90^\circ, 270^\circ$). The extremal values are found for integer multiples of $\theta = \arccos(1/\sqrt{3}) \approx 54.7356^\circ$, i.e., for the *magic angle*.

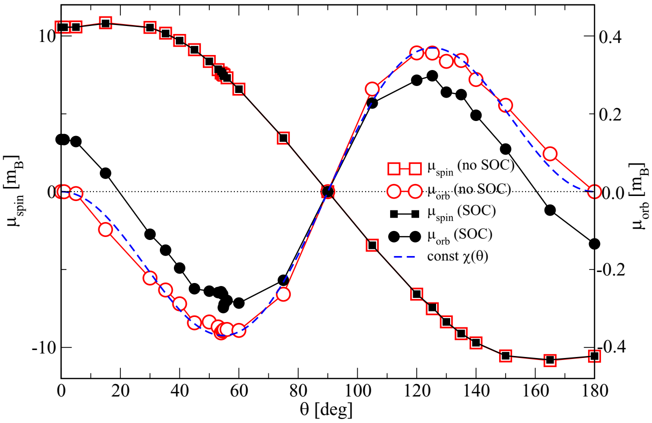

FIG. 5. Spin (squares) and orbital (circles) magnetic moments as a function of the polar angle θ in the noncoplanar chiral magnet ncpM0. Results including spin-orbit coupling (SOC) are shown as solid circles, and those for vanishing SOC are given as open circles. A fit of the latter to the scalar spin chirality $\chi(\theta)$ (see text) is shown as a dashed line.

Figure 6 shows spin and orbital moments for the structure ncpM9 as a function of the polar angle θ, again with and without spin-orbit coupling. For the spin moment (solid squares) spin-orbit coupling is, as to be expected, of negligible relevance. The orbital moment (open circles) again has

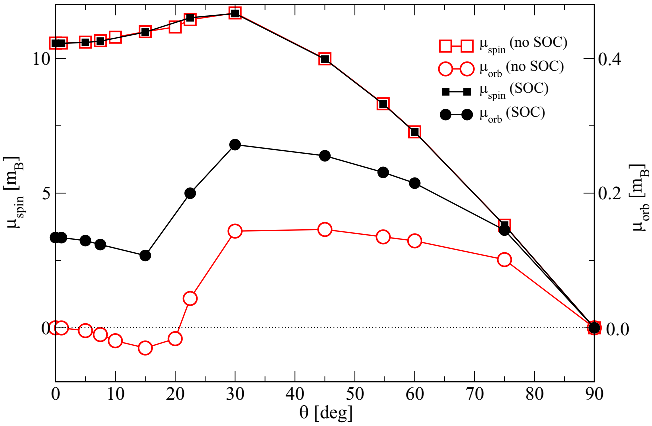

FIG. 6. Spin (squares) and orbital (circles) magnetic moments as a function of the polar angle θ in the noncoplanar achiral magnet ncpM9. Results including spin-orbit coupling (SOC) are shown as solid symbols, and those for vanishing SOC are given as open symbols.

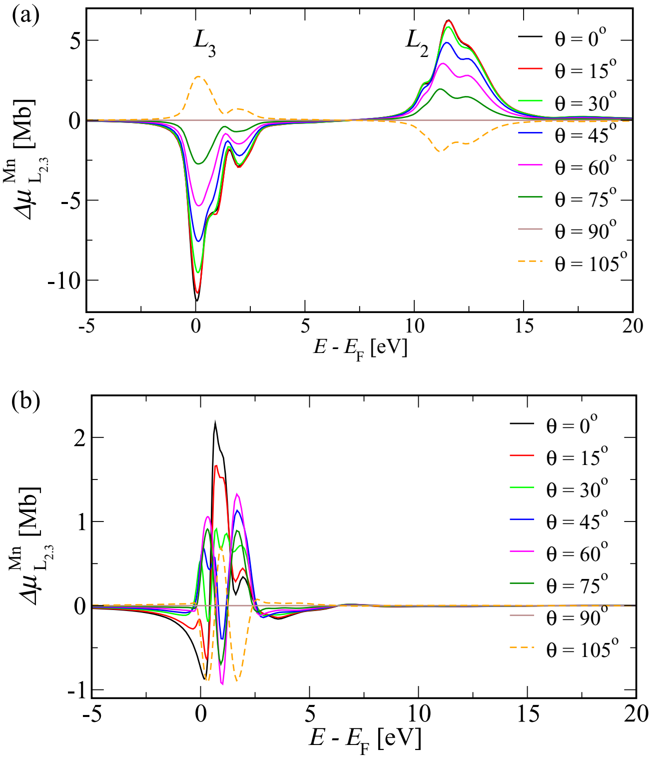

FIG. 7. X-ray magnetic circular dichroism spectra $\Delta\mu^{\mathrm{Mn}}_{L_{2,3}}$ at the Mn $L_{2,3}$ edge in the noncoplanar chiral magnetic structure ncpM0 with (a) and without (b) inclusion of spin-orbit coupling. The polar angle θ gives the tilt of the moments with respect to the [0001] direction, which coincides with the direction of the x-ray beam.

a large chirality-induced component, whose angular dependence however does not appear to be simply proportional to the scalar spin chirality. While the even symmetry around $\theta = 0^\circ$ and the odd symmetry around $\theta = 90^\circ$ are obeyed, the behavior in-between seems to be more complicated. At small angles θ the orbital moment is negative. Its magnitude increases with increasing θ in line with the case of the ncpM0 spin configuration, up to $\theta \approx 15^\circ$. When θ increases further, μ_{orb} changes sign, becoming positive, and after passing through a maximum again vanishes at $\theta = 90^\circ$. Note that, despite the global inversion symmetry connecting the two kagome sublattices, these have, as in the case of ncpM0, the same finite scalar spin chirality.

C. X-ray absorption spectra

X-ray absorption spectroscopy has a long and successful history concerning its application as a local probe to magnetic systems. In particular the so-called x-ray magnetic circular dichroism (XMCD) sum rules [80–82] allow one, for example, to deduce from the integrated $L_{2,3}$ spectra of $3d$-transition metals their spin and orbital magnetic moments. In line with the sum rules an angular dependence according to $\cos(\hat{m} \cdot \hat{q})$ is normally assumed, where $\hat{m}$ and $\hat{q}$ are the orientation of the local moment probed by XMCD and of the x-ray beam, respectively. This simple relation implies that in spin-compensated antiferromagnetic systems the XMCD should vanish. However, both XMCD [49] and the magneto-optic Kerr effect [37,47] are, in fact, due to their relation to the frequency-dependent conductivity tensor [74], expected to be observable in any magnetic structure that allows for a finite anomalous Hall conductivity.

In order to elucidate whether also the chirality-induced orbital moment discussed in Sec. III B can be deduced from x-ray absorption as suggested by dos Santos Dias *et al.* [25], we perform first-principles calculations of XAS spectra as a function of polar angle θ. The XMCD signals in the noncoplanar magnetic structure ncpM0 including and excluding spin-orbit coupling are shown in Figs. 7(a) and 7(b), respectively. The absorption for incidence along the [0001] direction is calculated for the $L_{2,3}$ edge of Mn and summed over all sites of the unit cell. Suppressing spin-orbit coupling obviously leads to a degeneracy of the $2p$ initial states; i.e., it removes in particular the spin-orbit splitting into $2p_{1/2}$ and $2p_{3/2}$ shells. Accordingly only one edge is visible in Fig. 7(b), which nevertheless shows an XMCD signal. In both cases the strength of the signal is decreasing with increasing θ and is antisymmetric with respect to reversal of the global z component of the magnetization. The same applies to the XMCD spectra for the achiral structure ncpM9 in Fig. 8. Here the fine structure at the L_2-edge is slightly different from that in ncpM0 for the fully relativistic spectra (see Figs. 8(a) vs 7(a)) and quite so for the non-relativistic ones (Figs. 8(b) vs 7(b)).

As the XMCD signal is determined by both spin and orbital magnetic moment, a clear-cut decomposition is desirable in order to assess the chirality-induced contribution to the latter by x-ray absorption spectroscopy. Since the standard XMCD sum rules cannot be applied here and their generalization to noncollinear magnetic order is still on open issue, an approximate scheme following the proposal in Ref. [25] has been employed. Figures 9 and 10 show the difference between the average x-ray adsorption spectroscopy (XAS) and the XMCD signals for the field-aligned (ferromagnetic, FM, $\theta = 0^\circ$) limit and the noncollinear structures with $\theta \neq 0^\circ$ in ncpM0 and ncpM9, respectively. As stated above, this follows the proposed protocol of dos Santos Dias *et al.*

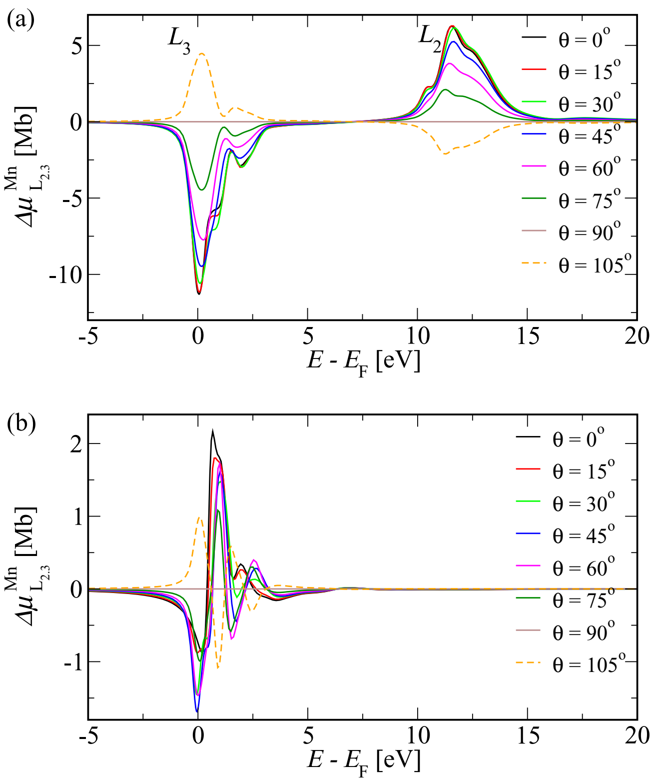

FIG. 8. X-ray magnetic circular dichroism spectra $\Delta\mu^{\mathrm{Mn}}_{L_{2,3}}$ at the Mn $L_{2,3}$ edge in the noncoplanar achiral magnetic structure ncpM9 with (a) and without (b) inclusion of spin-orbit coupling. The polar angle θ gives the tilt of the moments with respect to the [0001] direction, that coincides with the direction of the x-ray beam.

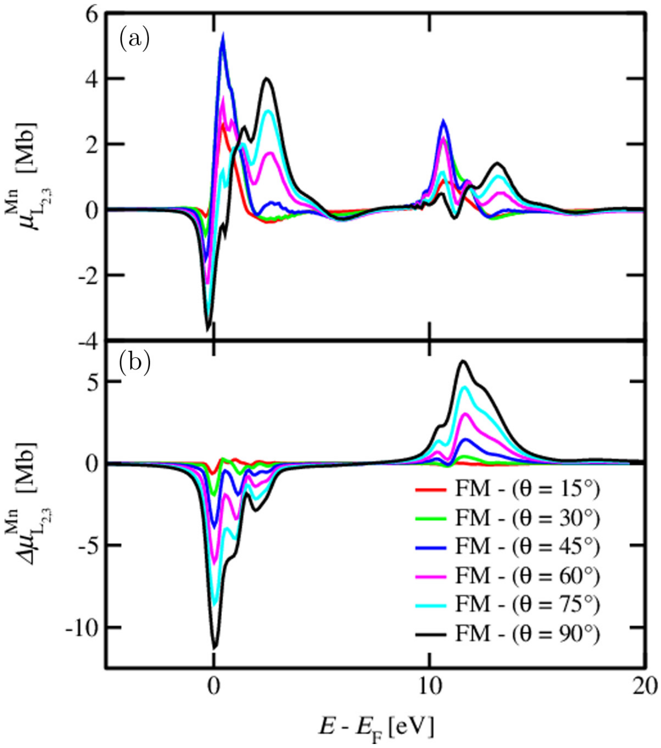

FIG. 9. Difference between ferromagnetic and noncollinear polarization-averaged XAS spectra (a) and x-ray magnetic circular dichroism (XMCD) spectra (b) at the Mn $L_{2,3}$ edge in the chiral magnetic structure ncpM0. The polar angle θ gives the tilt of the moments with respect to the [0001] direction.

[25], devised for magneto-optical experiments on skyrmionic systems. A remaining obstacle is, however, the assessment of the spin-moment-induced contribution for which a linear and spin-texture-independent relation to the polar angle has been assumed by these authors. Obviously an unambiguous separation into spin- and orbital- as well as spin-orbit- and chirality-induced contributions is duly needed. Note that due to the simplified assumption of a collinear arrangement of moments the standard XMCD rules certainly have to be revised in order to make full use of the proposed procedure.

D. Transport results: (T)AHE and (T)SHE

Results for the anomalous Hall conductivity σ_{xy} as a function of θ are shown in Fig. 11(a) for ncpM0. As can be seen, both anomalous Hall conductivity (AHC) and the chirality-induced or topological contribution σ^T_{xy} obtained in the nonrelativistic limit $c_0/c \to 0$ (see the Appendix) are antisymmetric or odd with respect to magnetization reversal around $\theta = 90^\circ$. The chirality-induced component is clearly not simply proportional to the scalar spin chirality (see Fig. 5), similar to the observation made by Hanke *et al.* [26] for γ-FeMn. The largest values for σ^T_{xy} are, for example, found for $\theta = 60^\circ$ and 120° and not for the magic angle. In addition we observe two sign changes between the coplanar antiferromagnetic structure ($\theta = 90^\circ$) and the ferromagnetic states at $\theta = 0^\circ$ and 180°. In these limits σ^T_{xy} vanishes and the AHC is purely spin-orbit induced. Note that the calculations were performed for the finite temperature $T = 300$ K that was accounted for by uncorrelated lattice displacements via the so-called alloy analogy model [83]. This was done in order to circumvent the numerical difficulties arising for the $\vec{k}$-space integration for perfectly ordered systems. However, as it turns out, the conductivities are almost entirely intrinsic in nature in the sense of negligible impact of the so-called vertex corrections associated with the thermally induced disorder. Accordingly it is the band structure that determines the angular dependence of the AHC, or expressed alternatively its Berry curvature [84,85], as skew scattering contributions arising from the presence of impurities [86] or locally correlated fluctuating spins [87] are not considered here. As the Berry curvature is usually more pronounced near avoided band crossings, the latter may have a crucial role for the AHE conductivity if they are located near the Fermi energy. To compare the SOC-induced and chirality-induced modifications of the electronic structure around the Fermi energy, Fig. 12 represents the spin-resolved Bloch spectral function calculated for the FM configuration, without (top panels) and with (middle panels) SOC, as well as for the ncpM0 configuration with $\theta = 10^\circ$, without SOC (bottom panels). Obviously, avoided band crossings that have a different origin occur at a different place in the band structure. Moreover, the chirality-induced avoided band crossings depend on the angle θ, contributing that way to the θ-dependent topological Hall conductivity via the energy bands in the vicinity of E_F. However, the chirality-induced emergent magnetic field B_{eff} that implies breaking of time-

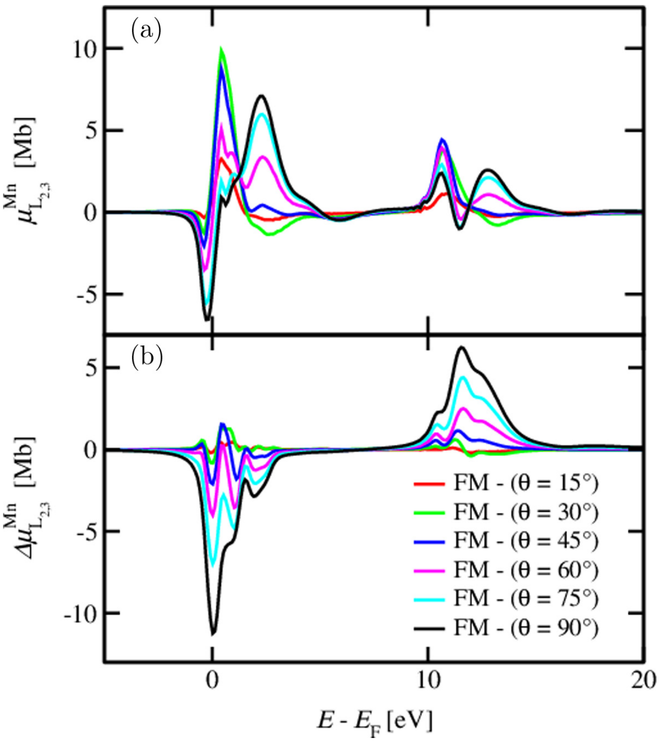

FIG. 10. Difference between ferromagnetic and noncollinear polarization-averaged XAS spectra (a) and x-ray magnetic circular dichroism (XMCD) spectra (b) at the Mn $L_{2,3}$ edge in the achiral magnetic structure ncpM9. The polar angle θ gives the tilt of the moments with respect to the [0001] direction.

reversal symmetry for the system is nonvanishing only for $\chi_{ijk} \neq 0$; i.e., a nonvanishing THE occurs only for the case of a nonzero scalar spin chirality [30,88], but it is absent for $\theta = 90^\circ$. The spin Hall conductivity in the relativistic and nonrelativistic limits, σ_{xy}^{z} and $\sigma_{xy}^{z,T}$, given in of Fig. 11(b) is even with respect to magnetization reversal around antiferromagnetic configuration at $\theta = 90^\circ$. It is strongly dependent on the noncoplanar spin texture and quite differently so for its spin-orbit- and chirality-induced contributions. Comparing the θ dependence of the topological AHE and SHE conductivities (open squares), one can see a correlated occurrence of their minima and maxima at the same angles θ. This seems to reflect the fact that both effects are caused by the same mechanism connected with the avoided band crossings discussed above [89]. In the ferromagnetic case, i.e., for $\theta = 0^\circ$ and 180°, both topological contributions σ_{xy}^{T} and $\sigma_{xy}^{z,T}$ vanish. The chirality-induced emergent magnetic field B_{eff}, acting in opposite directions for the opposite spin channels, governs the transverse spin current leading to a nonzero TSHE [89]. However, a clear difference between the THE and the TSHE occurs at $\theta = 90^\circ$. While the THE is vanishing at this angle, the TSHE is still finite and has a rather large magnitude. This behavior may be compared to the property of paramagnetic materials that show no AHE but a SHE.

Finally, it should be mentioned that in Fig. 11 the total SHE conductivity is small but nonzero for the angles $\theta = 0^\circ$, 90°, and 180° because of its SOC-induced contribution.

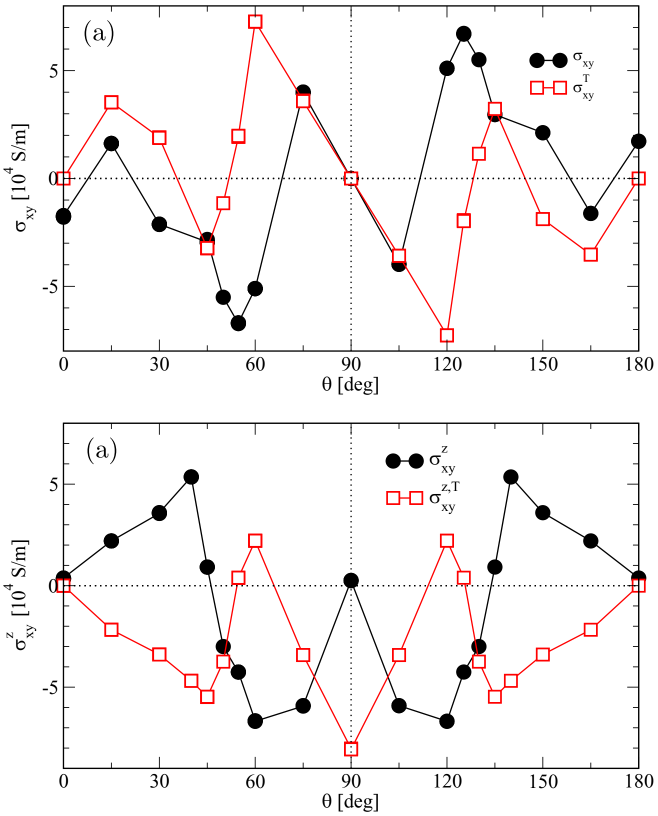

FIG. 11. (a) Anomalous Hall conductivity σ_{xy} and its chirality-induced or topological contribution σ_{xy}^{T} as functions of the polar angle θ in ncpM0. (b) Corresponding results for the (topological) spin Hall conductivity σ_{xy} ($\sigma_{xy}^{z,T}$).

Quite similar observations can be made in Fig. 13 for the achiral spin structure ncpM9 shown for the range $\theta = 0^\circ$–90°. As can be seen, the AHC in Fig. 13(a) is found to be antisymmetric (odd) with respect to magnetization reversal whereas the SHC in Fig. 13(b) is symmetric. The detailed angular dependence is distinct from that in ncpM0 for both quantities; i.e., the two hypothetical structures could be distinguished experimentally. We propose that the abundance of assumed spin configurations in hexagonal Mn_3X compounds could be confirmed or discarded via corresponding transport measurements rotating an applied magnetic field supported together with accompanying first-principles calculations.

The longitudinal charge transport is even with respect to magnetization reversal and anisotropic, i.e., $\sigma_{xx} = \sigma_{yy} \neq \sigma_{zz}$. In the absence of spin-orbit coupling and the associated anisotropic magnetoresistance, the anisotropy of the spin texture and the bare-crystal-induced anisotropy already present in the nonmagnetic case remain. Similar observations can be reported for the longitudinal spin conductivities $\sigma_{xx}^{z} = \sigma_{yy}^{z} \neq \sigma_{zz}^{z}$, which however are odd with respect to magnetization reversal.

E. Spinorbitronic effects: (T)SOT and (T)EE

Naturally the question arises whether the so-called spinorbitronic phenomena spin-orbit torque (SOT) and Edelstein effect (EE) also exhibit chirality-induced contributions lead-

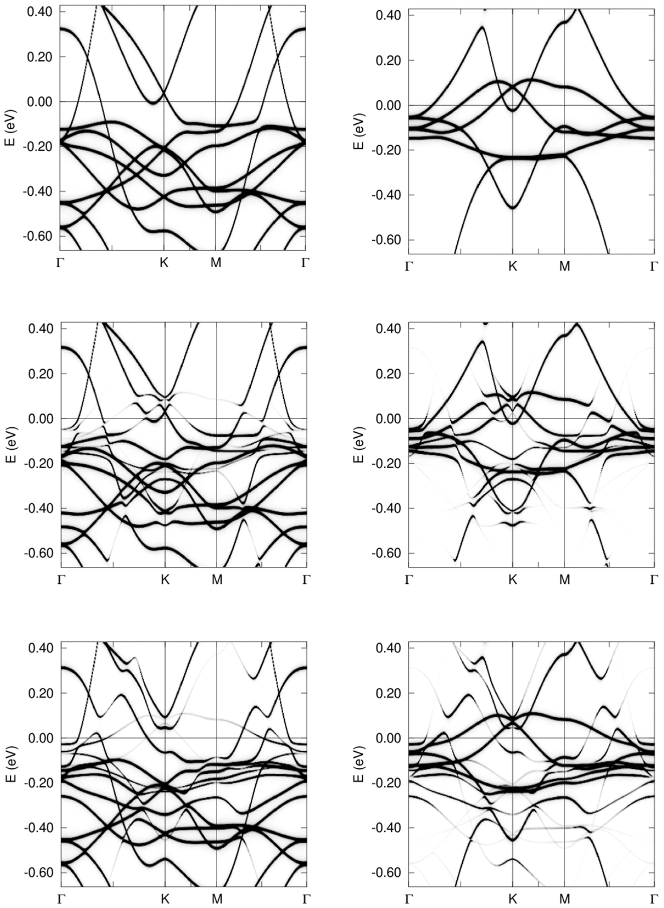

FIG. 12. Spin-resolved Bloch spectral function for the FM configuration, without SOC (top panels); for the FM configuration, with SOC (middle panels); and for the ncpM0 configuration with $\theta = 10^\circ$, without SOC (bottom panels). The left panels correspond to the spin-up states, and the right panels correspond to the spin-down states.

ing to finite values in the absence of spin-orbit coupling. Employing the same Kubo linear response framework used for the charge and spin transport calculations in the previous section, but exchanging the operator for the response, the (spin) current density operators, by either the magnetic torque operator [60] or the spin magnetization operator [61], the torkances t_{ij}, and Edelstein polarizations p_{ij} can be computed from first principles. Figure 14 shows the polar-angle dependence of the torkance tensor elements $t_{xx} = t_{yy}$ [panel (a)], $t_{xy} = -t_{yx}$ [panel (b)], and t_{zz} [panel (c)] in the chiral compound ncpM0. The diagonal torkances in Figs. 14(a) and 14(c) are obviously even with respect to magnetization reversal, i.e., symmetric with respect to $\theta = 90^\circ$, while the off-diagonal antisymmetric element $t_{xy} = -t_{yx}$ in Fig. 14(b) is odd. For this as well as for $t_{xx} = t_{yy}$, indeed, a sizable chirality-induced contribution is found that appears to be largest at $\theta = 30^\circ$ and 150°. The diagonal torkance t_{zz} in Fig. 14(c), corresponding to a rotation of the moments about the [0001] direction or the z axis coinciding with the direction of the applied electric field, is almost exclusively spin-orbit driven. In all three cases the full torkances vanish in the ferromagnetic limit ($\theta = 0^\circ$ and 180°) due to inversion symmetry. Note, however, that the off-diagonal elements vanish also for $\theta = 90^\circ$, despite a lack of the inversion symmetry in this case. This effect was discussed by Wimmer *et al.* [60], and Železný *et al.* [90] pointed out that the total torkance can vanish in noncentrosymmetric crystals if the sublattice torkances cancel each other.

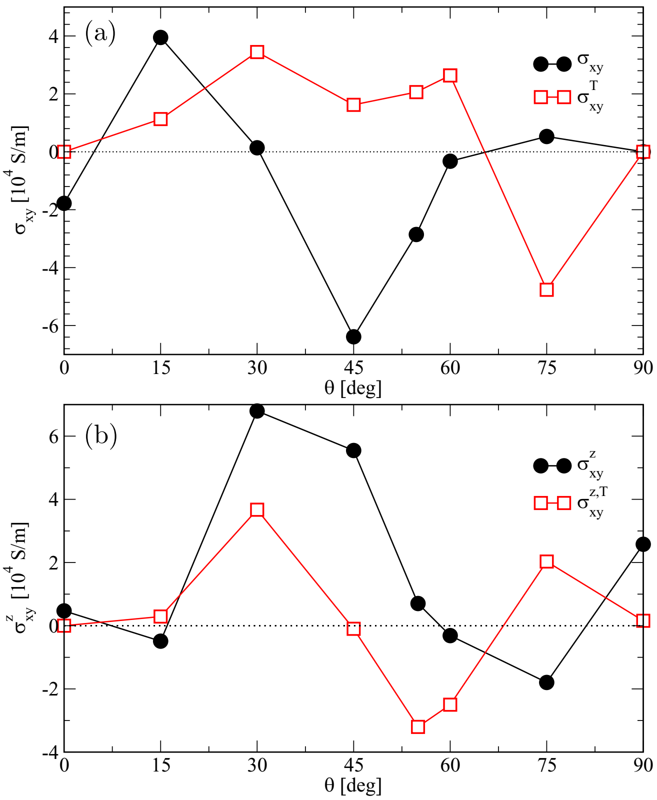

FIG. 13. (a) Anomalous Hall conductivity σ_{xy} and its chirality-induced or topological contribution σ^T_{xy} as functions of the polar angle θ in ncpM9. (b)_ Corresponding results for the (topological) spin Hall conductivity σ_{xy} ($\sigma^{z,T}_{xy}$).

The Edelstein polarization is one of the two microscopic mechanisms usually discussed as a source for the SOT, namely the (Rashba-)Edelstein torque, while the spin Hall torque is attributed to the spin-transfer-torque-like action of a spin-polarized current on the local magnetization. The elements of the corresponding Edelstein polarization tensor $\underline{\boldsymbol{p}}$ are shown in Fig. 15 as a function of the polar angle θ. The elements p_{ij} are found to behave very similarly to the corresponding elements of $\underline{\boldsymbol{t}}$; i.e., the diagonal elements are even, the off-diagonal ones are odd, and $p_{xx} = p_{yy}$ [Fig. 15(a)] and $p_{xy} = -p_{yx}$ [Fig. 15(b)] are overall chirality dominated while p_{zz} in the Fig. 15(c) is again essentially SOC induced. Note, however, that the correspondence between t_{ij} and p_{ij} is not trivial, as an additional cross product with the local magnetization is involved for the operator representing the response in the case of the torkance. This leads, for example, for the odd torkance $t_{xy} = -t_{yx}$ in Fig. 14(c) to a different angular dependence as compared to $p_{xy} = -p_{yx}$, in particular, close to the ferromagnetic limits at the left and right ends. For the topological contributions this is even more pronounced. While the odd Edelstein polarization is chirality dominated close to the antiferromagnetic configuration at $\theta = 90^\circ$, the SOT- and chirality-induced torkances are even of different signs here. The achiral coplanar and noncoplanar structures

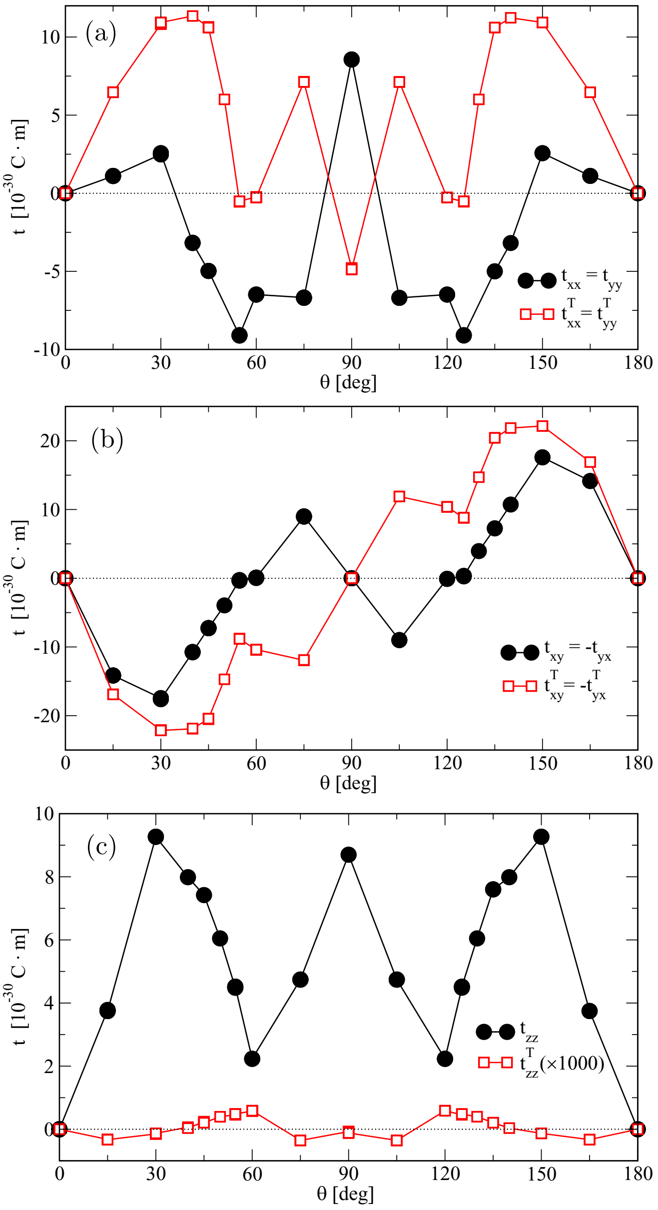

FIG. 14. Spin-orbit torkances $t_{xx} = t_{yy}$ (a), $t_{xy} = -t_{yx}$ (b), and t_{zz} (c) as functions of the polar angle θ in ncpM0. The chirality-induced contributions t_{ij}^T are given as open squares.

ncAFM9 and ncpM9 are found to be numerically zero as demanded by the inversion symmetry (see Sec III A).

F. Noncoplanar antiferromagnets

By rotating the moments in the two kagome planes in opposite directions by the same angle θ, noncoplanar antiferromagnetic structures as shown in Fig. 16 for $\theta = \pm 45^\circ$ are obtained. Figure 16(a) is derived from the coplanar AFM structure ncAFM0, while the ncpAFM9 structure in Figure 16(b) is obtained from the achiral ncAFM9 structure. As θ differs for both magnetic sublattices, the inversion symmetry is obviously broken; i.e., a chiral structure results. Note that, for ncpAFM0 inversion combined with time-reversal, $(\bar{1}')$ is still a symmetry operation.

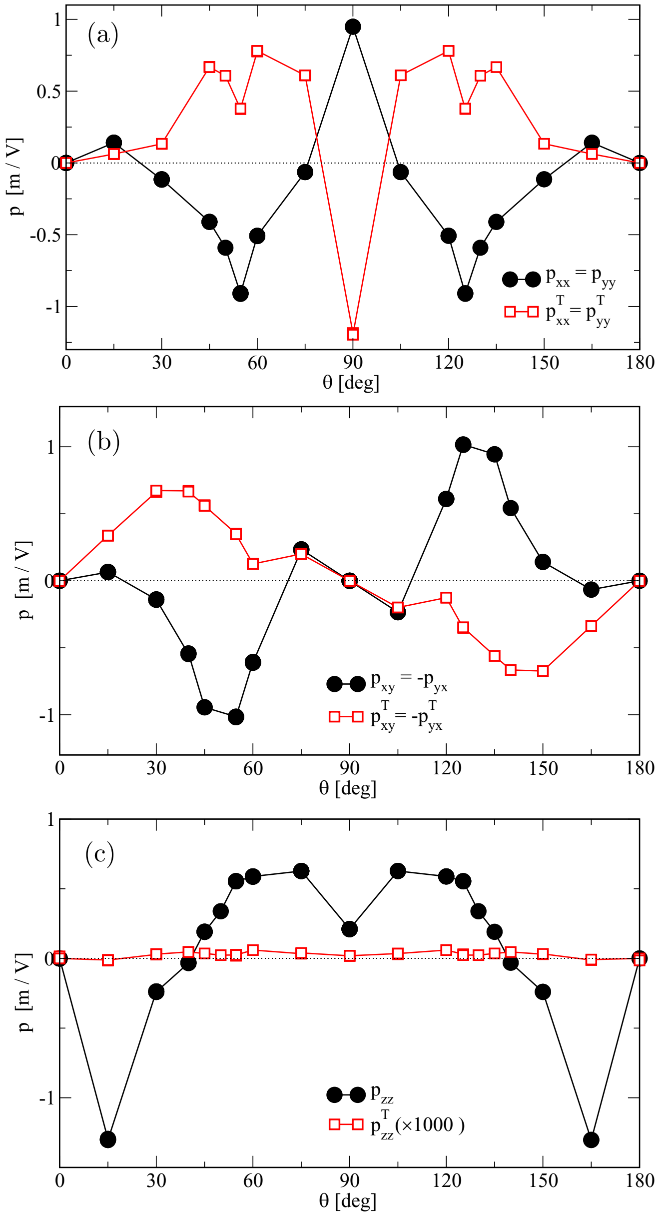

FIG. 15. Edelstein polarization tensor elements $p_{xx} = p_{yy}$ (a), $p_{xy} = -p_{yx}$ (b), and p_{zz} (c) as functions of the polar angle θ in ncpM0. The small chirality-induced contributions p_{ij}^T scaled by a factor of 1000 are given as open squares.

The tensor shapes for charge and z-polarized spin conductivity correspond for both structures to the nonmagnetic case; i.e., they are diagonal with $\sigma_{xx} = \sigma_{yy} \neq \sigma_{zz}$ and only one independent element of $\underline{\sigma}^z$, the spin Hall conductivity $\sigma^z_{xy} = -\sigma^z_{yx}$. The shapes of $\underline{\sigma}^x$ and $\underline{\sigma}^y$ for ncpAFM0 and ncpAFM9, however, differ from each other as well as from the ones for the NM structure [59]. For the torkance and the Edelstein polarization the tensor shapes are given in Eqs. (7) and (8). Obviously there is a finite Edelstein polarization as well as spin-orbit torkance present for both structures. However, the corresponding tensor shapes differ from each other, as the magnetic point group has to be considered here [60,61].

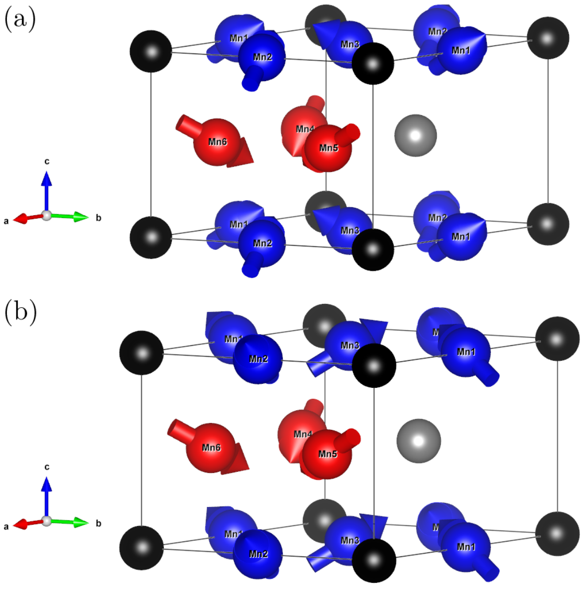

FIG. 16. Noncoplanar antiferromagnetic structures obtained from Fig. 3 by rotating the moments in the two kagome planes into opposite directions by the same angle. The structure in panel (a) has the same chirality in both sublattices (ncpAFM0), while in panel (b) they are of opposite sign (ncpAFM9) [77].

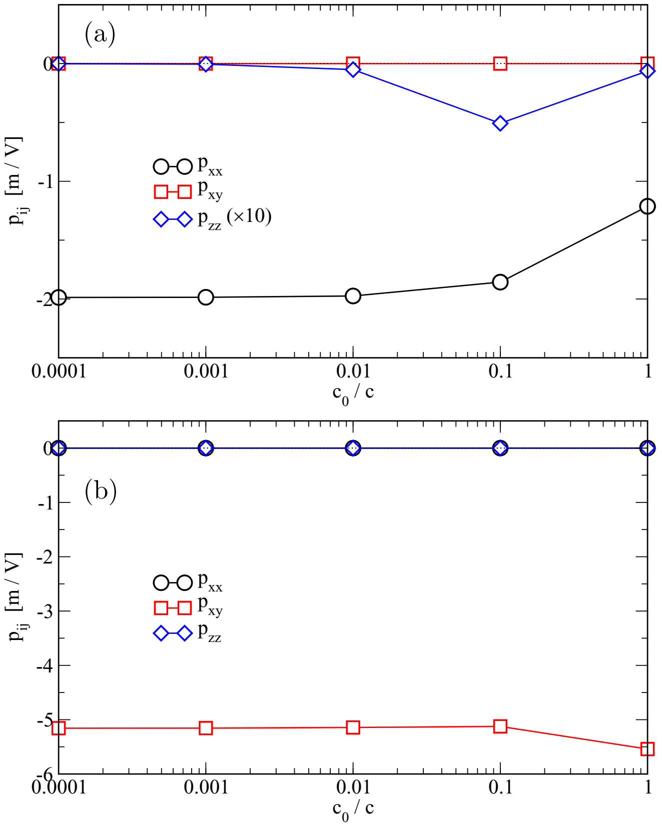

FIG. 17. Edelstein polarizations p_{xx}, p_{xy}, and p_{zz} in ncpAFM0 (a) and ncpAFM9 (b) as functions of c_0/c. For both structures the polar angle θ is 45° for one sublattice and 135° for the other sublattice. The relativistic limit is on the right ($c_0/c = 1$); the nonrelativistic one is on the left ($c_0/c \to 0$).

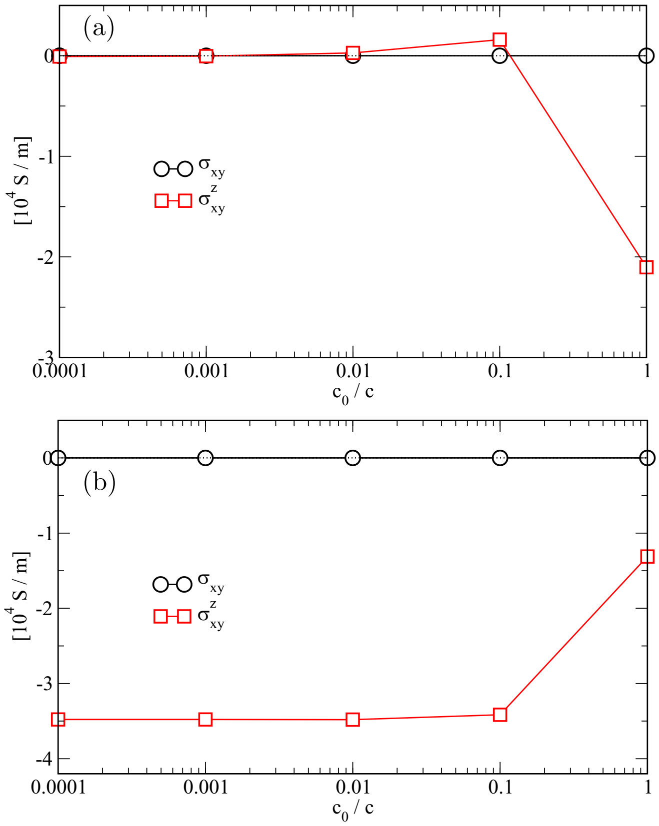

FIG. 18. Anomalous and spin Hall conductivities, σ_{xy} and σ^z_{xy}, respectively, in ncpAFM0 (a) and ncpAFM9 (b) as functions of c_0/c. For both structures the polar angle θ is 45°. The relativistic limit is on the right ($c_0/c = 1$); the nonrelativistic one is on the left ($c_0/c \to 0$).

Figure 17 shows the Edelstein polarization tensor elements p_{xx}, p_{xy}, and p_{zz} for both structures at $\theta = \pm 45°$ as a function of a scaled speed of light c (see the Appendix for details). Confirming the tensor shapes in Eqs. (7) and (8), in Fig. 17(a) only the diagonal elements are nonzero, while in the lower panel only p_{xy} is nonvanishing. Furthermore it can be stated that for ncpAFM0 again p_{zz} is smaller than p_{xx} and vanishes in the nonrelativistic limit ($c_0/c \to 0$), while p_{xx} has a large chirality-induced contribution. The antisymmetric Edelstein polarization p_{xy} for ncpAFM9 shown in Fig. 17(b) weakly depends on the c_0/c ratio, implying that it is almost exclusively arising from the spin texture.

In agreement with the absence of off-diagonal antisymmetric conductivity tensor elements, the XMCD signals of the two chiral magnetic sublattices cancel each other numerically exactly (not shown here). The same applies to the anomalous Hall conductivity shown in Fig. 18, while the spin Hall conductivities are found to be finite with either a vanishing (ncpAFM0) or a sizable topological contribution (ncpAFM9).

IV. CONCLUSIONS

To summarize, the effects of a noncollinear and a noncoplanar spin texture on orbital moments, x-ray absorption, charge and spin transport, as well as spin-orbit torque and Edelstein polarization, have been investigated by first-principles calculations for hexagonal $\mathrm{Mn_3Ge}$. By smoothly varying the polar angle with respect to the kagome planes of corner-sharing triangles in two hypothetical reference structures, one globally chiral and one achiral, the chirality-induced or topological contributions were compared to the spin-orbit-induced parts. To obtain the former in the absence of the latter, the nonrelativistic limit has been taken by scaling the speed of light c. The key findings are first of all the occurrences of topological orbital moments in the presence and the absence of global inversion symmetry, in the latter case following the angular dependence expected from the scalar spin chirality. A proposal of its experimental verification by XMCD measurements in a rotating external magnetic field is supported by a comparison of spectra for the field-aligned ferromagnetic case with those of noncoplanar spin configurations. Also here the limit of vanishing spin-orbit coupling has been investigated; conclusive statements could, however, not yet be made due to limitations of the standard XMCD sum rules. Furthermore the presence, the angular dependence, and the magnitude of the chirality-induced contributions to the anomalous and spin Hall conductivities have been demonstrated. Similar calculations of the spin-orbit torkance and the Edelstein polarization reveal sizable topological contributions also here, which can, depending on which quantity and which tensor element is considered as well as on the polar angle, enhance or suppress the spin-orbit-induced effects and be either dominating or vanishing.

Future studies on realistic noncollinear antiferromagnets of the hexagonal $\mathrm{Mn_3}X$ type with X = Ga, Ge, or Sn based on the experimentally assumed or theoretically proposed spin structures could help in determining the actual configuration and the relevance of chirality-induced contributions in measured response properties. A proposed extension of the XMCD sum rules to noncollinear magnetic order and the absence of spin-orbit coupling should be able to support experimental efforts on the quantification of topological orbital moments.

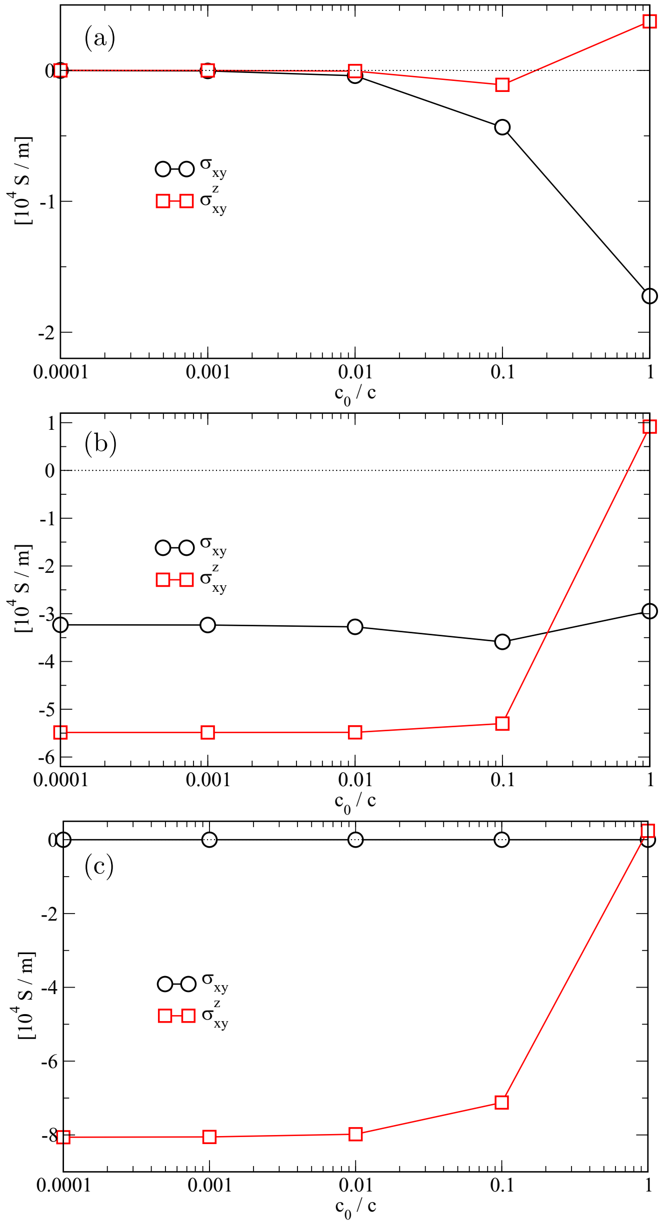

FIG. 19. Anomalous and spin Hall conductivity as a function of c_0/c in the ferromagnetic state (a), the noncoplanar chiral magnetic state ncpM0 (b) for $\theta = 45^\circ$, and the coplanar noncollinear chiral state ncAFM0 (c). The relativistic limit is on the right ($c_0/c = 1$); the nonrelativistic one is on the left ($c_0/c \to 0$).

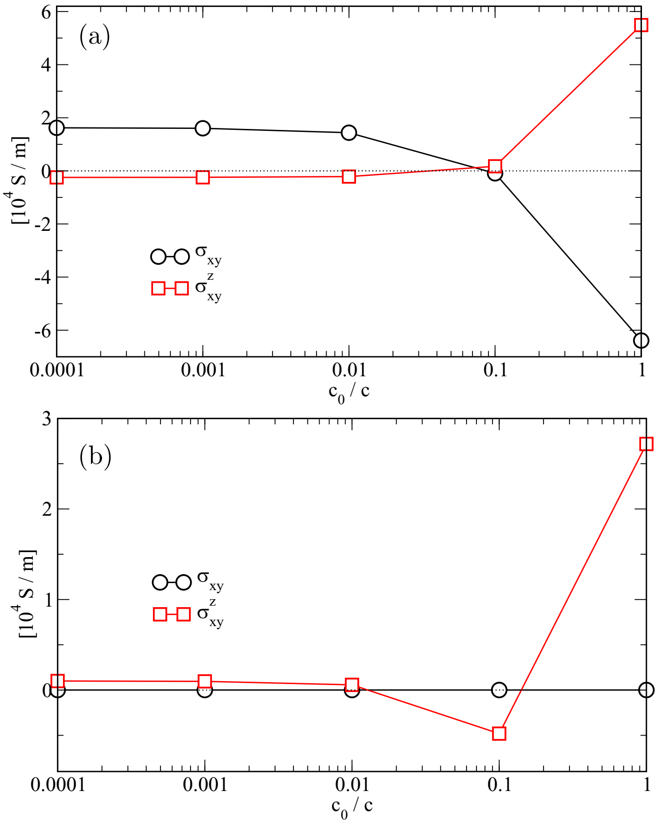

FIG. 20. Anomalous and spin Hall conductivity as a function of c_0/c in the noncoplanar achiral magnetic state ncpM9 (a) for $\theta = 45^\circ$, and the coplanar noncollinear achiral state ncAFM9 (b). The relativistic limit is on the right ($c_0/c = 1$); the nonrelativistic one is on the left ($c_0/c \to 0$).

ACKNOWLEDGMENT

Financial support by the DFG via SFB 1277 (*Emergente Relativistische Effekte in der Kondensierten Materie*) is gratefully acknowledged.

APPENDIX: MANIPULATING THE SPIN-ORBIT COUPLING

The topological contributions to the various response quantities discussed were determined by either setting the spin-orbit coupling explicitly to zero in the self-consistent calculations (when dealing with the orbital magnetic moment) or by scaling the speed of light c in the x-ray absorption and Kubo linear response calculations. The limit $c_0/c \to 0$ with the speed of light in vacuum c_0, or equivalently $c/c_0 \to \infty$, corresponds to the nonrelativistic case. Obviously not only the spin-orbit coupling is affected this way, but also the so-called scalar-relativistic effects. However, for the properties relevant to this work the spin-orbit coupling is the relevant relativistic correction.

Figure 19 shows the anomalous (black symbols) and spin Hall (red symbols) conductivities as a function of the scaled speed of light c_0/c for the ferromagnetic state [panel (a)], the noncoplanar magnetic state ncpM0 depicted in Fig. 4(a) [panel (b)], and the coplanar noncollinear antiferromagnetic state ncAFM0 [panel (c)]. Going from the relativistic limit on the right side to the nonrelativistic limit on the left, both σ_{xy} and σ_{xy}^z vanish for the ferromagnet, revealing their purely SOC-driven nature. In the noncoplanar magnetic state ($\theta = 45^\circ$) in Fig. 19(b), both are finite for $c_0/c \to 0$; i.e., they exhibit a chirality-induced or topological contribution arising from the spin texture. For both quantities this is sizable. The anomalous Hall conductivity [Fig. 19(b) depends weakly on the c_0/c ratio, implying that the contribution due to the so-called topological Hall effect (THE) is dominating in the relativistic limit. The topological spin Hall effect (TSHE) is of opposite sign when compared to the SOC-induced contribution. For the noncollinear antiferromagnetic structure ncAFM0 [Fig. 19(c)], the anomalous Hall effect vanishes due to symmetry [see Table I and Eq. (1)], while the SHE governed by the SOC (in the case of a noncollinear antiferromagnetic structure) has again the sign opposite to that for the TSHE and is much smaller in magnitude.

Corresponding results for the structures ncpM9 (again for $\theta = 45^\circ$) and ncAFM9 are presented in Fig. 20. Here the relation of chirality- and SOC-induced contributions is somewhat different. The former is (much) smaller for the AHE (SHE) and of opposite sign for both effects in the noncoplanar magnetic structure [Fig 20(a)]. In the coplanar antiferromagnetic state [Fig. 20(b)], the AHE is again vanishing, whereas the SHE is again predominantly SOC induced.

[1] M. Bode, M. Heide, K. von Bergmann, P. Ferriani, S. Heinze, G. Bihlmayer, A. Kubetzka, O. Pietzsch, S. Blügel, and R. Wiesendanger, Nature (London) **447**, 190 (2007).

[2] C. Train, R. Gheorghe, V. Krstic, L.-M. Chamoreau, N. S. Ovanesyan, G. L. J. A. Rikken, M. Gruselle, and M. Verdaguer, Nat. Mater. **7**, 729 (2008).

[3] H.-B. Braun, Adv. Phys. **61**, 1 (2012).

[4] J. Stein, M. Baum, S. Holbein, T. Finger, T. Cronert, C. Tölzer, T. Fröhlich, S. Biesenkamp, K. Schmalzl, P. Steffens, C. H. Lee, and M. Braden, Phys. Rev. Lett. **119**, 177201 (2017).

[5] C. S. Spencer, J. Gayles, N. A. Porter, S. Sugimoto, Z. Aslam, C. J. Kinane, T. R. Charlton, F. Freimuth, S. Chadov, S. Langridge, J. Sinova, C. Felser, S. Blügel, Y. Mokrousov, and C. H. Marrows, Phys. Rev. B **97**, 214406 (2018).

[6] T. Skyrme, Nucl. Phys. **31**, 556 (1962).

[7] S. Mühlbauer, B. Binz, F. Jonietz, C. Pfleiderer, A. Rosch, A. Neubauer, R. Georgii, and P. Böni, Science **323**, 915 (2009).

[8] A. Neubauer, C. Pfleiderer, B. Binz, A. Rosch, R. Ritz, P. G. Niklowitz, and P. Böni, Phys. Rev. Lett. **102**, 186602 (2009); **110**, 209902(E) (2013).

[9] S. Heinze, K. von Bergmann, M. Menzel, J. Brede, A. Kubetzka, R. Wiesendanger, G. Bihlmayer, and S. Blugel, Nat. Phys. **7**, 713 (2011).

[10] B. Dupe, M. Hoffmann, C. Paillard, and S. Heinze, Nat. Commun. **5**, 4030 (2014).

[11] H. Reichlová, D. Kriegner, V. Holý, K. Olejník, V. Novák, M. Yamada, K. Miura, S. Ogawa, H. Takahashi, T. Jungwirth, and J. Wunderlich, Phys. Rev. B **92**, 165424 (2015).

[12] C. Moreau-Luchaire, C. Moutafis, N. Reyren, J. Sampaio, C. A. F. Vaz, N. Van Horne, K. Bouzehouane, K. Garcia, C. Deranlot, P. Warnicke, P. Wohlhüter, J.-M. George, M. Weigand, J. Raabe, V. Cros, and A. Fert, Nat. Nanotechnol. **11**, 444 (2016).

[13] S. Woo, K. Litzius, B. Krüger, M.-Y. Im, L. Caretta, K. Richter, M. Mann, A. Krone, R. M. Reeve, M. Weigand, P. Agrawal, I. Lemesh, M.-A. Mawass, P. Fischer, M. Kläui, and G. S. D. Beach, Nat. Mater. **15**, 501 (2016).

[14] A. K. Nayak, V. Kumar, T. Ma, P. Werner, E. Pippel, R. Sahoo, F. Damay, U. K. Rößler, C. Felser, and S. S. P. Parkin, Nature (London) **548**, 561 (2017).

[15] X. Z. Yu, N. Kanazawa, W. Z. Zhang, T. Nagai, T. Hara, K. Kimoto, Y. Matsui, Y. Onose, and Y. Tokura, Nat. Commun. **3**, 988 (2012).

[16] J. Sampaio, V. Cros, S. Rohart, A. Thiaville, and A. Fert, Nat. Nanotechnol. **8**, 839 (2013).

[17] A. Fert, V. Cros, and J. Sampaio, Nat. Nanotechnol. **8**, 152 (2013).

[18] R. Tomasello, E. Martinez, R. Zivieri, L. Torres, M. Carpentieri, and G. Finocchio, Sci. Rep. **4**, 6784 (2014).

[19] A. Fert, N. Reyren, and V. Cros, Nat. Rev. Mater. **2**, 17031 (2017).

[20] W. Koshibae and N. Nagaosa, Nat. Commun. **7**, 10542 (2016).

[21] R. Shindou and N. Nagaosa, Phys. Rev. Lett. **87**, 116801 (2001).

[22] K. Nakamura, T. Ito, and A. J. Freeman, Phys. Rev. B **68**, 180404(R) (2003).

[23] M. Hoffmann, J. Weischenberg, B. Dupé, F. Freimuth, P. Ferriani, Y. Mokrousov, and S. Heinze, Phys. Rev. B **92**, 020401(R) (2015).

[24] J.-P. Hanke, F. Freimuth, A. K. Nandy, H. Zhang, S. Blügel, and Y. Mokrousov, Phys. Rev. B **94**, 121114(R) (2016).

[25] M. dos Santos Dias, J. Bouaziz, M. Bouhassoune, S. Blügel, and S. Lounis, Nat. Commun. **7**, 13613 (2016).

[26] J.-P. Hanke, F. Freimuth, S. Blügel, and Y. Mokrousov, Sci. Rep. **7**, 41078 (2017).

[27] Y. Taguchi, Y. Oohara, H. Yoshizawa, N. Nagaosa, and Y. Tokura, Science **291**, 2573 (2001).

[28] G. Tatara and H. Kawamura, J. Phys. Soc. Jpn. **71**, 2613 (2002).

[29] M. Onoda and N. Nagaosa, J. Phys. Soc. Jpn. **71**, 19 (2002).

[30] P. Bruno, V. K. Dugaev, and M. Taillefumier, Phys. Rev. Lett. **93**, 096806 (2004).

[31] T. Tomizawa and H. Kontani, Phys. Rev. B **82**, 104412 (2010).

[32] T. Schulz, R. Ritz, A. Bauer, M. Halder, M. Wagner, C. Franz, C. Pfleiderer, K. Everschor, M. Garst, and A. Rosch, Nat. Phys. **8**, 301 (2012).

[33] N. Nagaosa and Y. Tokura, Nat. Nanotechnol. **8**, 899 (2013).

[34] C. Franz, F. Freimuth, A. Bauer, R. Ritz, C. Schnarr, C. Duvinage, T. Adams, S. Blügel, A. Rosch, Y. Mokrousov, and C. Pfleiderer, Phys. Rev. Lett. **112**, 186601 (2014).

[35] G. Yin, Y. Liu, Y. Barlas, J. Zang, and R. K. Lake, Phys. Rev. B **92**, 024411 (2015).

[36] P. M. Buhl, F. Freimuth, S. Blügel, and Y. Mokrousov, Phys. Status Solidi RRL **11**, 1700007 (2017).

[37] H. Chen, Q. Niu, and A. H. MacDonald, Phys. Rev. Lett. **112**, 017205 (2014).

[38] J. Kübler and C. Felser, Europhys. Lett. **108**, 67001 (2014).

[39] Y. Zhang, Y. Sun, H. Yang, J. Železný, S. P. P. Parkin, C. Felser, and B. Yan, Phys. Rev. B **95**, 075128 (2017).

[40] D. Boldrin and A. S. Wills, Adv. Condens. Matter Phys. **2012**, 615295 (2012).

[41] C. Sürgers, G. Fischer, P. Winkel, and H. v. Löhneysen, Nat. Commun. **5**, 3400 (2014).

[42] S. Nakatsuji, N. Kiyohara, and T. Higo, Nature (London) **527**, 212 (2015).

[43] N. Kiyohara, T. Tomita, and S. Nakatsuji, Phys. Rev. Appl. **5**, 064009 (2016).

[44] A. K. Nayak, J. E. Fischer, Y. Sun, B. Yan, J. Karel, A. C. Komarek, C. Shekhar, N. Kumar, W. Schnelle, J. Kübler, C. Felser, and S. S. P. Parkin, Sci. Adv. **2**, e1501870 (2016).

[45] C. Sürgers, T. Wolf, P. Adelmann, W. Kittler, G. Fischer, and H. v. Löhneysen, Sci. Rep. **7**, 42982 (2017).

[46] Z. H. Liu, Y. J. Zhang, G. D. Liu, B. Ding, E. K. Liu, H. M. Jafri, Z. P. Hou, W. H. Wang, X. Q. Ma, and G. H. Wu, Sci. Rep. **7**, 515 (2017).

[47] J. Orenstein and J. E. Moore, Phys. Rev. B **87**, 165110 (2013).

[48] W. Feng, G.-Y. Guo, J. Zhou, Y. Yao, and Q. Niu, Phys. Rev. B **92**, 144426 (2015).

[49] S. Wimmer, S. Mankovsky, J. Minár, A. N. Yaresko, and H. Ebert, Phys. Rev. B **100**, 214429 (2019).

[50] O. Gomonay, Phys. Rev. B **91**, 144421 (2015).

[51] J. Železný, Y. Zhang, C. Felser, and B. Yan, Phys. Rev. Lett. **119**, 187204 (2017).

[52] Y. Zhang, J. Železný, Y. Sun, J. van den Brink, and B. Yan, New J. Phys. **20**, 073028 (2018).

[53] J. B. S. Mendes, R. O. Cunha, O. Alves Santos, P. R. T. Ribeiro, F. L. A. Machado, R. L. Rodríguez-Suárez, A. Azevedo, and S. M. Rezende, Phys. Rev. B **89**, 140406(R) (2014).

[54] W. Zhang, W. Han, S.-H. Yang, Y. Sun, Y. Zhang, B. Yan, and S. S. P. Parkin, Sci. Adv. **2**, e1600759 (2016).

[55] G.-Y. Guo and T.-C. Wang, Phys. Rev. B **96**, 224415 (2017).

[56] M. Ikhlas, T. Tomita, T. Koretsune, M.-T. Suzuki, D. Nishio-Hamane, R. Arita, Y. Otani, and S. Nakatsuji, Nat. Phys. **13**, 1085 (2017).

[57] L. Šmejkal, Y. Mokrousov, B. Yan, and A. H. MacDonald, Nat. Phys. **14**, 242 (2018).

[58] W. H. Kleiner, Phys. Rev. **142**, 318 (1966).

[59] M. Seemann, D. Ködderitzsch, S. Wimmer, and H. Ebert, Phys. Rev. B **92**, 155138 (2015).

[60] S. Wimmer, K. Chadova, M. Seemann, D. Ködderitzsch, and H. Ebert, Phys. Rev. B **94**, 054415 (2016).

[61] S. Wimmer, Spin caloric transport and related phenomena from first principles, Ph.D. thesis, Ludwig-Maximilians-Universitaet Muenchen, 2018.

[62] H. T. Stokes, D. M. Hatch, and B. J. Campbell, ISOTROPY Software Suite, iso.byu.edu.

[63] H. T. Stokes and D. M. Hatch, J. Appl. Crystallogr. **38**, 237 (2005).

[64] R. Kubo, Can. J. Phys. **34**, 1274 (1956).

[65] R. Kubo, J. Phys. Soc. Jpn. **12**, 570 (1957).

[66] W. H. Butler, Phys. Rev. B **31**, 3260 (1985).

[67] A. Crépieux and P. Bruno, Phys. Rev. B **64**, 014416 (2001).

[68] D. Ködderitzsch, K. Chadova, and H. Ebert, Phys. Rev. B **92**, 184415 (2015).

[69] T. Tanaka, H. Kontani, M. Naito, T. Naito, D. S. Hirashima, K. Yamada, and J. Inoue, Phys. Rev. B **77**, 165117 (2008).

[70] T. Naito, D. S. Hirashima, and H. Kontani, Phys. Rev. B **81**, 195111 (2010).

[71] S. Lowitzer, D. Ködderitzsch, and H. Ebert, Phys. Rev. Lett. **105**, 266604 (2010).

[72] S. Lowitzer, M. Gradhand, D. Ködderitzsch, D. V. Fedorov, I. Mertig, and H. Ebert, Phys. Rev. Lett. **106**, 056601 (2011).

[73] H. Ebert *et al.*, The Munich SPR-KKR package, http://olymp.cup.uni-muenchen.de/ak/ebert/SPRKKR.

[74] H. Ebert, Rep. Prog. Phys. **59**, 1665 (1996).

[75] P. Středa, J. Phys. C: Solid State Phys. **15**, L717 (1982).

[76] J. Banhart, A. Vernes, and H. Ebert, Solid State Commun. **98**, 129 (1996).

[77] This figure has been created using the software VESTA [91].

[78] D. Zhang, B. Yan, S.-C. Wu, J. Kübler, G. Kreiner, S. S. P. Parkin, and C. Felser, J. Phys.: Condens. Matter **25**, 206006 (2013).

[79] T. Hahn (Ed.), *International Tables for Crystallography, Volume A: Space Group Symmetry* (Springer, Berlin, 2002).

[80] J. L. Erskine and E. A. Stern, Phys. Rev. B **12**, 5016 (1975).

[81] B. T. Thole, P. Carra, F. Sette, and G. van der Laan, Phys. Rev. Lett. **68**, 1943 (1992).

[82] P. Carra, B. T. Thole, M. Altarelli, and X. Wang, Phys. Rev. Lett. **70**, 694 (1993).

[83] H. Ebert, S. Mankovsky, K. Chadova, S. Polesya, J. Minár, and D. Ködderitzsch, Phys. Rev. B **91**, 165132 (2015).

[84] M. V. Berry, Proc. R. Soc. London, Ser. A **392**, 45 (1984).

[85] D. Xiao, M.-C. Chang, and Q. Niu, Rev. Mod. Phys. **82**, 1959 (2010).

[86] K. Nakazawa and H. Kohno, J. Phys. Soc. Jpn. **83**, 073707 (2014).

[87] H. Ishizuka and N. Nagaosa, Sci. Adv. **4**, aap9962 (2018).

[88] G. Tatara, H. Kohno, J. Shibata, Y. Lemaho, and K.-J. Lee, J. Phys. Soc. Jpn. **76**, 054707 (2007).

[89] I. V. Rozhansky, K. S. Denisov, M. B. Lifshits, N. S. Averkiev, and E. Läderanta, Phys. Status Solidi B **256**, 1900033 (2019).

[90] J. Železný, H. Gao, A. Manchon, F. Freimuth, Y. Mokrousov, J. Zemen, J. Mašek, J. Sinova, and T. Jungwirth, Phys. Rev. B **95**, 014403 (2017).

[91] K. Momma and F. Izumi, J. Appl. Crystallogr. **44**, 1272 (2011).